Local structural plasticity of the *Staphylococcus aureus* evasion protein EapH1 enables engagement with multiple neutrophil serine proteases

Received for publication, March 26, 2020, and in revised form, April 16, 2020 Published, Papers in Press, April 17, 2020, DOI 10.1074/jbc.RA120.013601

Timothy J. Herdendorf[‡], Daphne A. C. Stapels[§], Suzan H. M. Rooijakkers[§], and Brian V. Geisbrecht[‡1]

From the [‡]Department of Biochemistry & Molecular Biophysics, Kansas State University, Manhattan, Kansas 66506 and the [§]Department of Medical Microbiology, University Medical Center Utrecht, 3584 CX Utrecht, The Netherlands

Edited by Wolfgang Peti

Members of the EAP family of *Staphylococcus aureus* immune evasion proteins potently inhibit the neutrophil serine proteases (NSPs) neutrophil elastase, cathepsin-G, and proteinase-3. Previously, we determined a 1.8 Å resolution crystal structure of the EAP family member EapH1 bound to neutrophil elastase. This structure revealed that EapH1 blocks access to the enzyme's active site by forming a noncovalent complex with this host protease. To determine how EapH1 inhibits other NSPs, we studied here the effects of EapH1 on cathepsin-G. We found that EapH1 inhibits cathepsin-G with a K_i of 9.8 ± 4.7 nM. Although this K_i value is ~466-fold weaker than the K_i for EapH1 inhibition of neutrophil elastase, the time dependence of inhibition was maintained. To define the physical basis for EapH1's inhibition of cathepsin-G, we crystallized EapH1 bound to this protease, solved the structure at 1.6 Å resolution, and refined the model to R_{work} and R_{free} values of 17.4% and 20.9%, respectively. This structure revealed a protease-binding mode for EapH1 with cathepsin-G that was globally similar to that seen in the previously determined EapH1–neutrophil elastase structure. The nature of the intermolecular interactions formed by EapH1 with cathepsin-G differed considerably from that with neutrophil elastase, however, with far greater contributions from the inhibitor backbone in the cathepsin-G–bound form. Together, these results reveal that EapH1's ability to form high-affinity interactions with multiple NSP targets is due to its remarkable level of local structural plasticity.

Neutrophils are the most abundant leukocytes in the human body and serve essential roles in the cell-mediated innate immune response to bacteria (1). Although neutrophils normally circulate in an inactive state, they undergo significant physiological changes upon activation and phagocytosis of opsonized bacterial cells (2, 3). Maturation of the neutrophil phagosome is a stepwise process and involves fusion of the phagosomal compartment with several types of cytosolic granules that provide the biochemical tools necessary for efficiently killing the bacteria trapped within. The most prevalent type of granules, commonly referred to as "azurophilic" granules, contain large stores of antibacterial peptides and proteins. They include enzymes such as myeloperoxidase (MPO),[2] which converts H_2O_2 into cytotoxic hypohalous acids (*e.g.* HOCl) (4), as well as a series of chymotrypsin-like serine proteases, collectively known as neutrophil serine proteases (NSPs) (5–7). Although MPO and the oxidants it produces kill engulfed bacteria through altogether distinct mechanisms from those of NSPs, some studies have demonstrated that these systems may work synergistically within the phagosome (8). Thus, the concerted action of MPO and NSPs can be considered a cornerstone of bacterial killing within the neutrophil phagosome.

There are three canonical members of the NSP family of proteases: neutrophil elastase (NE), cathepsin-G (CG), and proteinase-3 (PR3) (5). A fourth member of this family, denoted NSP-4, has also been identified and characterized (9). The precise contributions of the various NSPs to bacterial killing appear to vary depending upon the nature of the pathogen and remain to be fully elucidated (1, 7). NSP substrate specificities also vary widely both *in vitro* and in physiological settings (7, 10). Despite this, NSPs as enzymes share many biochemical features with one another (5, 7). NE, CG, and PR3 can each be inhibited by the serpin α-1-antitrypsin as well as Chelonianin-class protease inhibitors (5, 11). X-ray crystallography studies have likewise revealed considerable structural homology between NE (12), CG (13), PR3 (14), and more recently NSP-4 (15), even though they share relatively modest levels of sequence identity (7). For example, whereas the mature polypeptides of human NE and CG are only 34% identical to one another, their crystal structures superimpose with a Cα RMSD value of 0.647 Å for the 158 of 204 positions that correspond and lie within a boundary of 5.0 Å following alignment (Fig. 1). These observations argue for a common ancestry to NSPs, even

This work was supported by National Institutes of Health Grants AI111203 and GM121511 (to B. V. G.). The authors declare that they have no conflicts of interest with the contents of this article. The content is solely the responsibility of the authors and does not necessarily represent the official views of the National Institutes of Health.

The atomic coordinates and structure factors (code 6VTM) have been deposited in the Protein Data Bank (http://wwpdb.org/).

This article contains Figs. S1–S4.

[1] To whom correspondence should be addressed: Dept. of Biochemistry and Molecular Biophysics, Kansas State University, 141 Chalmers Hall, 1711 Claflin Rd., Manhattan, KS 66506. Tel.: 785-532-3154; Fax: 785-532-7278; E-mail: GeisbrechtB@ksu.edu.

[2] The abbreviations used are: used in this article: MPO, myeloperoxidase; NSP, neutrophil serine protease; NE, neutrophil elastase; CG, cathepsin-G; PR3, proteinase-3; EAP, extracellular adherence protein repeat; Eap, *S. aureus* extracellular adherence protein; EapH1, *S. aureus* Eap homolog 1; EapH2, *S. aureus* Eap homolog 2; RMSD, root-mean-square deviation; SA_2PF-pNA, succinyl-Ala-Ala-Pro-Phe-*p*-nitroanilide; PDB, Protein Data Bank.

© 2020 Herdendorf et al. Published under exclusive license by The American Society for Biochemistry and Molecular Biology, Inc.

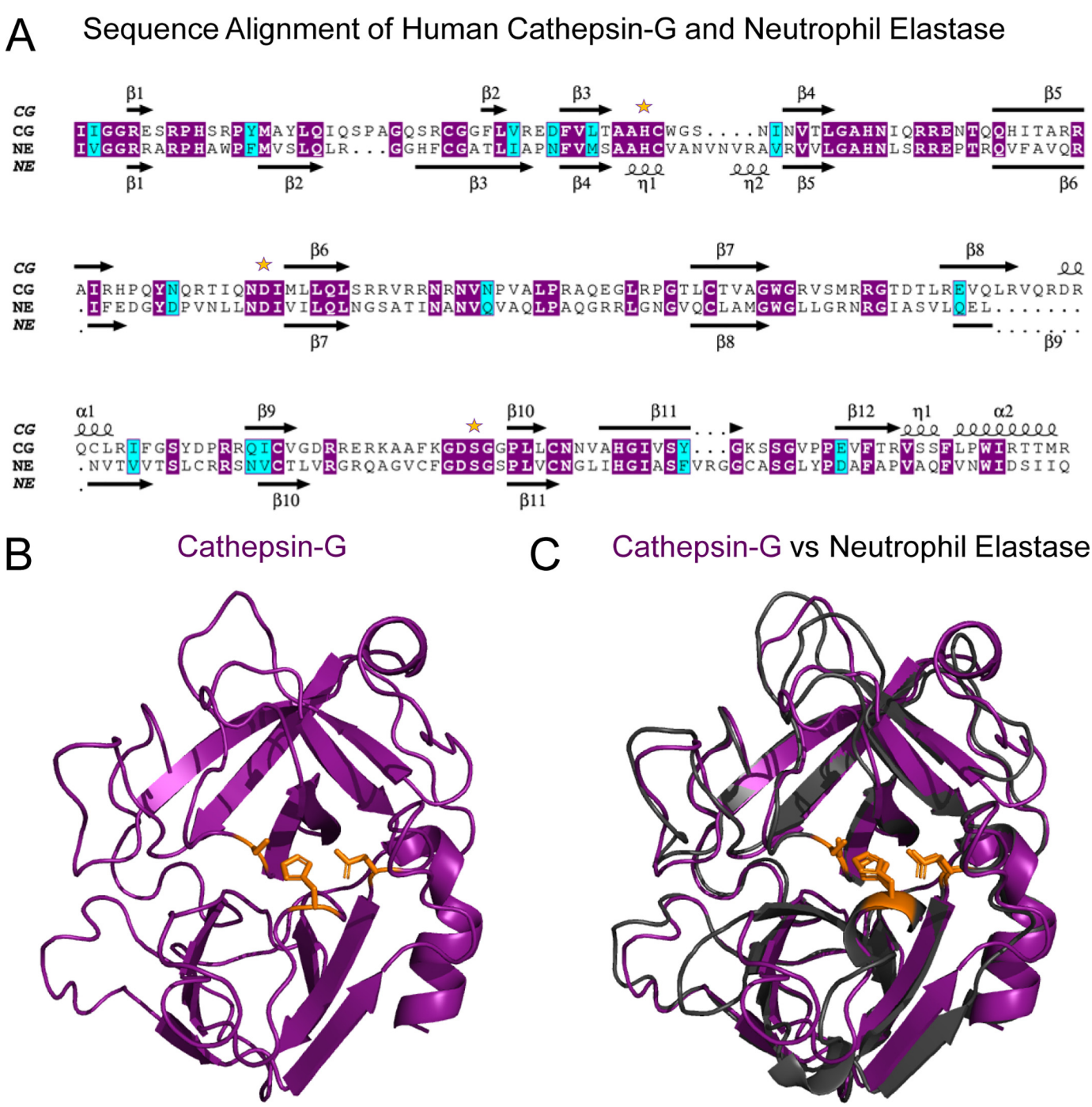

Figure 1. Sequence and structural comparisons of cathepsin-G and neutrophil elastase. *A*, the sequences of the matured serine protease domains of human CG and NE were aligned using Clustal Omega. Identical residues are shown in *purple blocks*, whereas chemically similar residues are shown in *cyan blocks*. Secondary structure elements for each protease are included above and below their respective sequences. The positions of the catalytic triad residues are denoted by a *star*. *B*, ribbon diagram representation of a human CG crystal structure. The catalytic triad residues are shown in ball-and-stick convention and are colored *orange*. *C*, structural superposition of CG (*purple*) and NE (*black*). The catalytic triads of both proteases are colored *orange*. Images of protein structures were rendered from the PDB entries 1CGH (13) and 1HNE (12) for CG and NE, respectively.

though the repertoire of phagosomal killing mechanisms has diversified throughout the evolution of the immune system.

Invading bacteria are quickly confronted by the host innate immune system. Consequently, there is heavy selective pressure for such organisms to evolve the capacity to disrupt, inhibit, or otherwise escape from the earliest steps of the innate immune response. In this regard, a large body of work has shown that the Gram-positive bacterium *Staphylococcus aureus* secretes an array of immune evasion proteins that interfere with the central processes of opsonophagocytosis and subsequent killing within the neutrophil phagosome (16–19). A small portion of phagocytosed *S. aureus* cells survive (20), lending support to the notion that the intraphagosomally acting *S. aureus* immune evasion program is at least somewhat protective to the bacteria. Indeed, our identification of *S. aureus* extracellular adherence domain proteins (EAPs) as highly

selective NSP inhibitors that promote bacterial virulence in several animal models is consistent with this hypothesis (21).

As with NSPs, there are likewise three canonical members of the *S. aureus* EAP protein family (22). The founding member of this family, Eap, is comprised of either four, five, or six tandem repeats of the so-called EAP domain depending upon the isoform (22, 23), whereas two homologs, denoted EapH1 and EapH2, contain only a single instance of this domain (22). The EAP domain adopts a β-grasp fold and consists of a prominent α-helix that spans essentially the entire diagonal dimension of a five-stranded, mixed β-sheet on which it is superimposed (22). As part of a larger effort to better define the *S. aureus* immune evasion program that acts inside the phagosome (*cf.* Ref. 24), we discovered and reported that Eap, EapH1, and EapH2 each potently inhibit all three canonical NSPs (21). Intriguingly, we also found that the inhibitory activity of EAP domain proteins is highly selective for NSPs (21). This stands in marked contrast to other physiological serine protease inhibitors, such as SERPINs (*e.g.* α-1-antitrypsin).

To better understand the physical basis behind NSP inhibition by EAP domain proteins, we solved a crystal structure of EapH1 bound to the most abundant NSP, NE (21). This structure revealed that EapH1 forms a highly complementary but noncovalent complex with NE that blocks substrate access to the protease active site (21). Interestingly, although a loop spanning EapH1 residues Val^{53} to Tyr^{63} is responsible for a large majority of the buried surface area at the NE/EapH1 interface, mutation of side chains in this region did not result in a noteworthy loss of EapH1 activity (25). Loss of EapH1 Arg^{89}, however, diminished EapH1 activity by nearly 15,000-fold (26). Subsequent studies showed that a second family member, EapH2, achieves inhibition of NE through an entirely different binding mode (25, 27), despite sharing ~50% sequence identity with EapH1. This series of results was most unexpected and raised questions about whether EapH1 relied on the same protease-binding mode to inhibit other NSPs. To address this central issue, we studied here the structural basis for inhibition of CG by EapH1.

Results

EapH1 is a reversible, time-dependent inhibitor of cathepsin-G

In our earlier work, we relied on a fluorometric assay to identify Eap, EapH1, and EapH2 as inhibitors of CG activity (21). However, to adapt our workflow to a more tractable approach, we developed and optimized a chromogenic method for assessing the kinetics and inhibition of CG activity. We determined the steady-state kinetic rate constants for turnover of the substrate SA_2PF-pNA by CG (Fig. S1). The k_{cat} and K_m values were estimated at 4.1 ± 0.9 s^{-1} and 2.1 ± 0.2 mM, respectively. We found that SA_2PF-pNA turnover by CG was described by a relatively high K_m value. As a consequence, certain studies required high concentrations of substrate that were not attainable without inclusion of DMSO as an additive in the assay buffer. To ensure that DMSO did not adversely impact CG activity, we determined the steady-state kinetic rate constants for the enzyme catalyzed reaction across a broad range of DMSO concentrations (Fig. S1). We found that DMSO levels approaching 30% (v/v) were tolerated by the enzyme and could be used to measure CG activity and its inhibition by EapH1.

Our previous studies of CG inhibition by EAP domain proteins made use of an enzyme/inhibitor preincubation step prior to substrate addition (21). However, when CG was exposed to various concentrations of substrate (*i.e.* SA_2PF-pNA) and inhibitor (*i.e.* EapH1) simultaneously, we found that the reaction progress curve was nonlinear in the presence of EapH1 (Fig. 2*A*). In contrast, when CG was preincubated with EapH1 and subsequently diluted with a solution containing a saturating concentration of substrate, we observed an initial lag phase that gradually transitioned to a steady-state rate (Fig. 2*A*). This demonstrated that EapH1 reversibly inhibits CG, similarly to its effect on NE (26).

As was the case for EapH1 inhibition of NE (26), EapH1 inhibition of CG was also defined by its time-dependent character. Because inhibition of this nature precludes using initial reaction velocities for detailed investigations, we opted to globally analyze CG reaction progress curves obtained across a range of enzyme, substrate, and inhibitor concentrations to define various aspects of CG inhibition by EapH1. We fit our experimental data to a rapid-equilibrium, competitive inhibition model (Scheme 1 and Table 1). According to this model, the microscopic rate constants pertaining to the CG mechanism should show good agreement regardless of the nature of the EapH1 inhibitor (*e.g.* WT *versus* a loss-of-function mutant). Indeed, the k_{cat} values (k_3) for cleavage of SA_2PF-pNA by CG in the presence of either WT EapH1 or its R89M mutant (26) were consistent with one another at 3.00 ± 0.82 and 2.51 ± 1.31 s^{-1}, respectively (Table 1). The substrate on rates (k_1; Table 1) were also well-matched at 1.70 ± 0.64 × 10^4 and 1.70 ± 0.31 × 10^4 M^{-1} s^{-1} for the WT and R89M mutant, respectively. Thus, the internal consistency of these rate constants suggested that global analysis of progress curves was suitable for assessing inhibition of CG activity by EapH1.

We previously determined that Arg^{89} is responsible for high-affinity binding of EapH1 to NE, because mutation of this side chain to methionine resulted in a 15,000-loss in K_i (26). In addition to this marked loss of function, we found that this mutation also abolished the time-dependent characteristic of NE inhibition (26). To more thoroughly understand CG inhibition by EapH1, we compared the macroscopic K_i values derived from progress curve analysis of WT and R89M forms of EapH1 (Table 1). WT EapH1 inhibited CG with a K_i of 9.8 ± 4.7 nM (Table 1 and Fig. 2*B*). This K_i value was ~466-fold weaker than what we previously determined for inhibition of NE by EapH1 (*i.e.* 21 ± 5 pM (26)). By contrast, the R89M mutant exhibited time-dependent inhibition of CG with a K_i of 980 ± 324 nM (Table 1 and Fig. 2*C*). This corresponded to a loss of 100-fold in K_i and suggested that the Arg^{89} side chain played a role in inhibition of CG. Nevertheless, the loss relative to the WT inhibitor was far less than the 15,000-fold we previously reported for inhibition of NE by the same mutant (26). Together, these observations suggested that the physical basis for EapH1 inhibition of CG might be fundamentally different than EapH1 inhibition of NE.

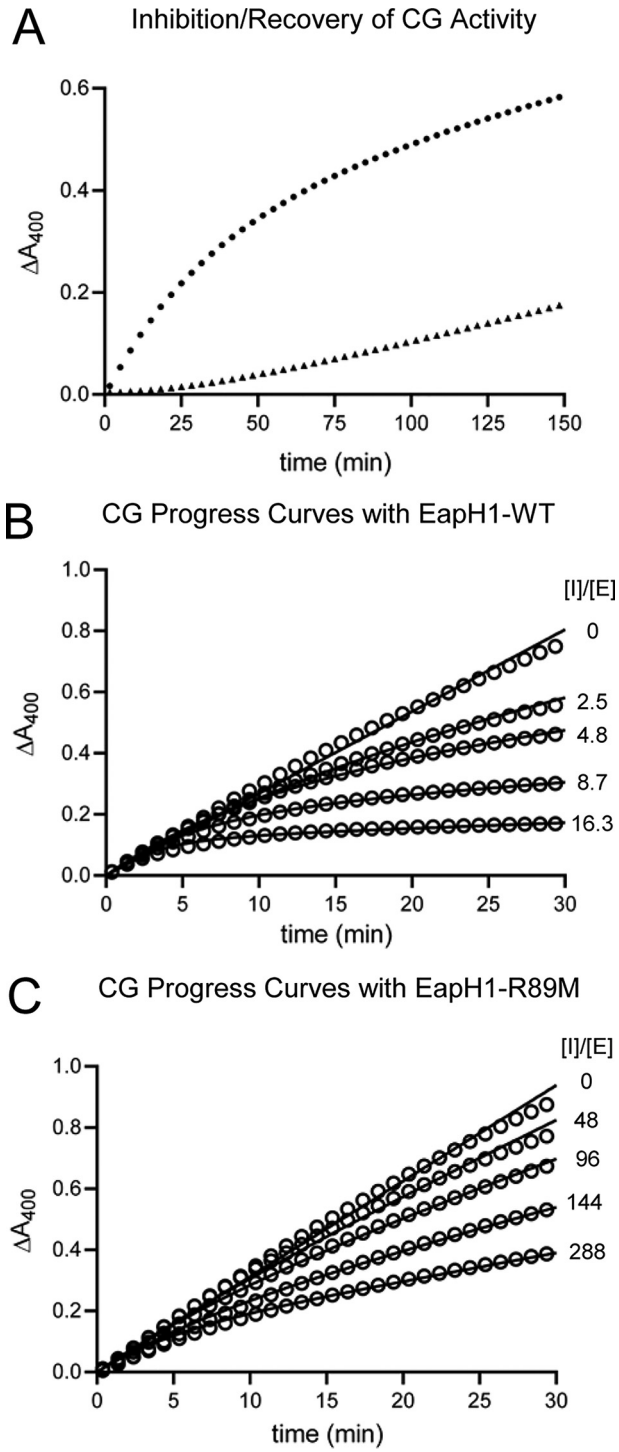

Figure 2. EapH1 is a time-dependent, reversible inhibitor of cathepsin-G. Cleavage of a chromogenic substrate by human CG was followed spectrophotometrically and was used to derive insight into inhibition of this reaction by EapH1. *A*, progress curves resulting from exposure of 10.2 nM CG to a solution containing 1.143 mM SA_2PF-pNA and 154 nM EapH1 (*filled circles*) or dilution of a preincubated CG/EapH1 sample with a solution of SA_2PF-pNA that gave identical final concentrations to the previous experiment (*filled triangles*). *B*, representative fitted progress curves for CG inhibition by EapH1-WT. *C*, representative fitted progress curves for CG inhibition by EapH1-R89M. The respective inhibitor to enzyme molar concentration ratios are *inset* at the *right-hand side* of *B* and *C*.

Table 1
Kinetic rate constant estimates determined by progress curve analysis
Microscopic rate constant estimates are the average of either six (EapH1-WT) or three (EapH1-R89M) individual sets of 30 progress curves (two [cathepsin-G], three [substrate] per [cathepsin-G], and five [inhibitor] per [substrate]. Progress curves were fit to a rapid equilibrium competitive inhibition model using KinTek Explorer (29). k_1/k_{-1} were linked and fixed at the determined steady-state substrate K_m.

	EapH1-WT		EapH1-R89M	
Rate constant	Value	S.D.	Value	S.D.
k_1 (M^{-1} s^{-1})	1.7×10^4	6.4×10^3	1.7×10^4	3.1×10^3
k_2 (s^{-1})	2.93	0.6	3.43	0.25
k_3 (s^{-1})	3.00	0.82	2.51	1.31
k_{-3} (M^{-1} s^{-1})	7.8×10^4	2.8×10^4	5.1×10^4	1.5×10^4
k_4 (M^{-1} s^{-1})	1.5×10^4	2.9×10^3	5.9×10^2	3.5×10^1
k_{-4} (s^{-1})	1.5×10^{-4}	7.5×10^{-5}	5.8×10^{-4}	1.7×10^{-4}
K_i (nM)	9.8	4.7	980	324

Crystal structure of cathepsin-G inhibited by EapH1 reveals a globally similar mode of NSP inhibition

We sought structural data to provide physical insight into our kinetic observations. Consequently, we crystallized EapH1 bound to human CG, solved the structure by molecular replacement, and refined the model to R_{work} and R_{free} values of 17.4 and 20.9%, respectively, at 1.6 Å limiting resolution (Table 2). The asymmetric unit of the crystal contained four copies of the CG/EapH1 complex (Fig. 3*A*). Our final model for each complex consisted of residues 16–238 of CG and residues 44–141 of EapH1, although residues 68–69 of the inhibitor could not be modeled because of poor map quality (please see "Experimental procedures" for additional details regarding the final model). Comparison of each complex revealed that they were essentially identical to one another (Fig. 3*B*), however, because the RMSDs of structural superpositions for all Cα residues were in no case greater than 0.178 Å. Consequently, we limited our subsequent analyses to the complex represented by chains A (CG) and B (EapH1) of the CG/EapH1 crystal structure (Fig. S2).

The fact that EapH1 inhibits CG in addition to NE raised questions about the protease-binding mode of EapH1 in these two complexes. Thus, we superimposed the CG/EapH1 structure upon that of NE/EapH1 to compare the position of the inhibitor in each state. We found that the structures of CG/EapH1 and NE/EapH1 shared a high level of global similarity to one another (Fig. 4*A*), as judged by a Cα RMSD value of 0.603 Å for the 239 of 305 positions that correspond and lie within a boundary of 5.0 Å following alignment. Not only were the positions of EapH1 relative to the target protease active site virtually identical, the positions of the EapH1 Cα atoms were also (Fig. 4*B*). These observations revealed that inhibition of CG and NE by EapH1 arises from a globally similar binding mode, regardless of the protease in question.

Target dependence of EapH1 interactions

Although the overall positioning of EapH1 was conserved in both the CG- and NE-bound states, the large difference in apparent K_i for these NSP targets suggested that significant differences were likely at the level of specific protein–protein interactions (Table 1 and Refs. 21, 26). We initially compared the buried surface area and shape complementarity of the CG/EapH1 complex with that of NE/EapH1 (21). Formation of

Table 2
X-ray diffraction data collection and refinement statistics
The values in parentheses are for the highest-resolution shell.

	CG/EapH1
Data collection	
Space group	*P* 1
Cell dimensions	
a, *b*, *c* (Å)	59.23, 72.90, 88.91
α, β, γ (°)	113.58, 91.17, 106.24
Resolution (Å)	34.34–1.60 (1.66–1.60)
R_{meas}	0.131 (1.009)
R_{pim}	0.068 (0.527)
$I/\sigma I$	10.3 (2.7)
$CC_{½}$	98.5 (63.9)
Completeness (%)	90.5 (89.6)
Redundancy	3.6 (3.4)
Refinement	
Resolution (Å)	34.34–1.60
No. reflections	148,710
R_{work}/R_{free}	17.4/20.9
No. atoms	11,262
Protein	10,160
Ligand/ion	65
Water	1,037
B-factors (Å^2)	
Protein	21.3
Ligand/ion	49.0
Water	31.1
RMSD	
Bond lengths (Å)	0.010
Bond angles (°)	1.13

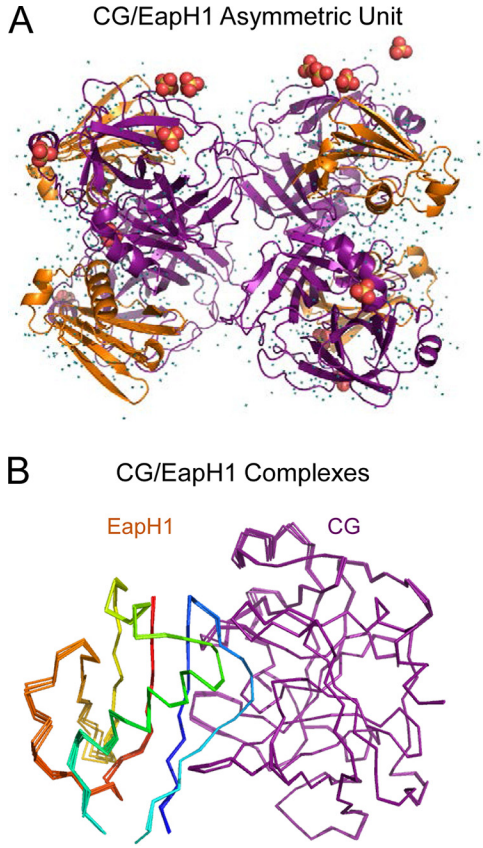

Figure 3. Crystal structure of cathepsin-G inhibited by EapH1 determined at 1.6 Å resolution. Human CG inhibited by EapH1 was crystallized, and the structure was solved by molecular replacement. *A*, ribbon representation of the final model for the asymmetric unit of the CG/EapH1 crystal (R_{free} = 20.9%). The four independent complexes of CG (*purple*) bound to EapH1 (*orange*) are shown with the proteins drawn as ribbon diagrams. The ordered solvent molecules are represented as *cyan asterisks*, whereas sulfate anions are shown as space-filling models (oxygen in *red*). *B*, structural superposition of the four CG/EapH1 complexes in the asymmetric unit. For the sake of clarity, only the Cα position of each protein residue is shown. CG proteins are colored *purple*, whereas EapH1 proteins are colored with the N terminus in *blue* and the C terminus in *red*. The chain break in each copy of EapH1 corresponds to two residues (Glu^{68} and Asn^{69}) that could not be modeled because of weak electron density.

the CG/EapH1 complex buried 1027.4 Å^2 of surface area from the inhibitor, which is 84.9 Å^2 greater than the 942.5 Å^2 of EapH1-derived surface buried in the NE/EapH1 complex (21). However, the surface complementarity statistic for CG/EapH1 was considerably lower at 0.73 when compared with 0.77 for NE/EapH1 (21). As with NE/EapH1, an overwhelming majority of the buried surface area from the inhibitor (*i.e.* 997.1 Å^2) arises from two main sites that resemble a pentagon on the EapH1 surface (Fig. 5, *A* and *B*). Site 1 consists of residues Tyr^{49}–Val^{65} that comprise the extended loop and second β-strand of EapH1. This site accounts for 768.3 Å^2. Aside from Ile^{51}, which is largely inaccessible in the EapH1 structure, 16 of the remaining 17 residues in this sequence appear to contribute to binding. Site 2 consists of residues Lys^{80}–Thr^{92}. These comprise the latter half of the large α-helix that is a defining structural feature of the EAP domain (22). Compared with site 1, site 2 accounts for far less buried surface area at 228.8 Å^2. Although only 8 of the 13 residues in this region appear to contribute to binding, this is most likely due to conformational restrictions arising from the large α-helix therein.

We also examined the intermolecular contacts at the CG/EapH1 interface and compared them to NE/EapH1. We focused our attention on Arg^{89}, which lies at the center of site 2 (Fig. 5, *A* and *B*), because mutation of this residue to methionine caused an ~100-fold loss in K_i relative to WT EapH1 (Table 1 and Fig. 2). The Arg^{89} side chain participates in two intermolecular hydrogen bonds with the backbone carbonyl oxygens of Gln^{97} and Arg^{98} from CG (Fig. 5*C* and Fig. S3). This arrangement essentially mirrors the role of Arg^{89} in the NE/EapH1 structure (Fig. 5*D* and Fig. S3). However, the presence of an additional hydrogen bond between the carbonyl oxygen of Gly^{90} and the Arg^{98} side chain of CG may partly explain the mild loss in K_i for CG exhibited by the EapH1-R89M mutant (Fig. 5*C* and Fig. S3).

Whereas the central features of Site 2 were largely the same in the CG- and NE-bound states of EapH1, we identified noteworthy differences in both the contributing positions and the extent of the hydrogen bonds and polar interaction network between site 1 of EapH1 and the target protease (Fig. 5, *E* and *F*, and Fig. S4). The backbone nitrogen and carbonyl oxygen of Thr^{57}, Leu^{59}, and Arg^{61}, which comprise the core of site 1, each form at least two hydrogen bonds with residues in the vicinity of the CG catalytic serine (*i.e.* Ser^{196}). Although a similar arrangement exists in the NE/EapH1 complex, the backbone nitrogen of EapH1 Leu^{59} also forms hydrogen bond of 3.1 Å distance with the side chain of the CG catalytic serine (Fig. 5*E*). A similar interaction is not seen in the NE-bound structure because the NE catalytic serine is modeled in rotamer that is not conducive to hydrogen bond formation (Fig. 5*F*). Aside from this, residues both N-terminal (*i.e.* Thr^{50} and Gly^{55}) and C-terminal (*i.e.* Tyr^{63} and Val^{65}) to the core of site 1 also participate in polar interactions with groups from CG. Such interactions are not seen in the NE-bound structure, which instead appears to

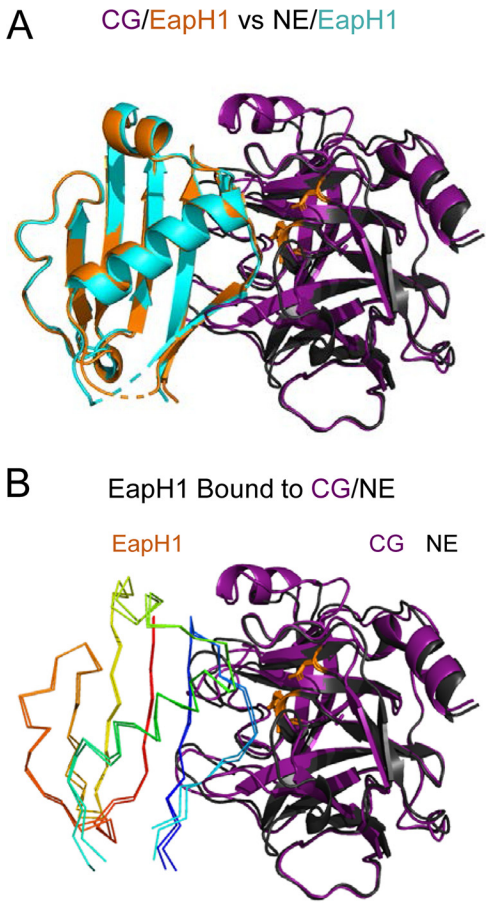

Figure 4. EapH1 inhibits cathepsin-G and neutrophil elastase through a globally similar binding mode. Crystal structures of CG/EapH1 and NE/EapH1 were superimposed to allow for a physical comparison of the EapH1 protease binding modes. *A*, a ribbon diagram of CG (*purple*) bound to EapH1 (*orange*) superimposed with that of NE (*black*) bound to EapH1 (*cyan*). The catalytic triads of both proteases are colored *orange* and drawn in ball-and-stick convention as a point of reference. *B*, an identical image to *A*, except that both copies of EapH1 are shown as only Cα positions with the N terminus in *blue* and the C terminus in *red*. The chain break in each copy of EapH1 corresponds to two residues (Glu^{68} and Asn^{69}) that could not be modeled in either structure because of weak electron density. Images of the NE/EapH1 structure were rendered from PDB entry 4NZL (21).

involve a higher level of hydrophobic interactions (Fig. S4). Finally, perhaps the most striking feature of site 1 observed by comparing these two structures is the extent of backbone-derived hydrogen bonds in the CG-bound state (Fig. 5, *E* and *F*). Equivalent interactions are not seen in the NE/EapH1 complex. In conclusion, comparison of these two structures reveals that although the overall binding mode is conserved, a high level of local structural plasticity underlies the ability of EapH1 to potently inhibit multiple NSPs.

Discussion

Although *S. aureus* expresses three different EAP domain proteins that act as high-affinity NSP inhibitors (7, 21), a majority of our molecular level understanding on how EAP proteins exhibit this function has come from studies on EapH1 (21, 25, 26). In this investigation, we expanded upon our previous work on EapH1 by characterizing the kinetics and structural basis for its inhibition of CG. We found that EapH1 acts both reversibly and time-dependently on CG (Fig. 2). We also found that the K_i value obtained by globally fitting a series of colorimetric assay reaction progress curves (*i.e.* 9.8 ± 4.7 nM) was in good agreement to that previously reported for a fluorescence-based method (*i.e.* 4.2 ± 2.2 nM) (21). Although these results confirmed that EapH1 inhibited GG with low-nanomolar potency (Table 1), the ~466-fold weaker K_i value for CG, when compared to NE, strongly suggested that there might be significant physical differences between the CG/EapH1 and NE/EapH1 complexes. Indeed, although our 1.6 Å resolution cocrystal structure of CG/EapH1 (Fig. 3) revealed a globally similar binding mode and comparable buried surface area to that of NE/EapH1 (Fig. 4), the overall surface complementarity of the CG/EapH1 complex (0.73) was considerably lower than that of NE/EapH1 (0.77). We also found substantial differences in both the nature and extent of the interactions formed by EapH1 with each target protease (Fig. 5). Most strikingly, there was a far greater number of EapH1 backbone-derived hydrogen bonds within the CG/EapH1 complex when compared with NE/EapH1 (Fig. 5). This not only demonstrated a remarkable level of local structural plasticity on the part of EapH1, it also provided further evidence on the versatility of EAP domains as protein–protein interaction scaffolds.

We previously determined that residue Arg^{89} of EapH1 plays an essential role in mediating high-affinity, time-dependent inhibition of NE (26). This side chain forms two intermolecular hydrogen bonds with carbonyls derived from the NE backbone, both of which are ≤3.0 Å in length (Fig. 5). Even though human CG shares only 34% identity with human NE (Fig. 1), we found an essentially equivalent pair of intermolecular hydrogen bonds between the Arg^{89} side chain and protease backbone carbonyls in the CG/EapH1 structure (Fig. 5). Although the K_i values for EapH1-R89M were comparable at 321 ± 12 nM for NE and 980 ± 324 nM for CG, the magnitude of the overall loss of function relative to WT EapH1 was far greater for NE (~15,000-fold) than it was for CG (~100-fold) (21). We believe this observation reflects more about the incredibly potent inhibition of NE by EapH1 (K_i = ~21 ± 5 pM) rather than a deficiency of its inhibition of CG (K_i = ~9.8 ± 4.7 nM), which is still quite potent in its own right. In the past, we have extensively used site-directed mutagenesis to define the functional contributions of various residues within EAP domain proteins, particularly as it pertains to inhibition of NSPs (25–27). Unfortunately, we noted that nearly all the specificity-driving interactions between EapH1 and CG appear to directly involve backbone atoms from the inhibitor (Fig. 5). Thus, we believe it is unlikely that an isosteric substitution mutant within either site 1 or site 2 of EapH1 could be constructed that is more diminished than EapH1-R89M (Fig. 5).

Recognizing that it is important to describe the differences between EapH1 in both its CG- and NE-bound states, we feel it is equally valuable to identify the similarities between these two complexes. Whereas the most obvious is that EapH1 uses a conserved binding mode to recognize both CG and NE (Fig. 4), we have noted several other structural features in common. First, EapH1 Leu^{59} makes a very close approach to the catalytic serine of both NSPs (Fig. 5, *E* and *F*, and Fig. S4). Although only the CG/EapH1 structure indicates the presence of a hydrogen bond between the backbone nitrogen of Leu^{59} and the catalytic

ASBMB

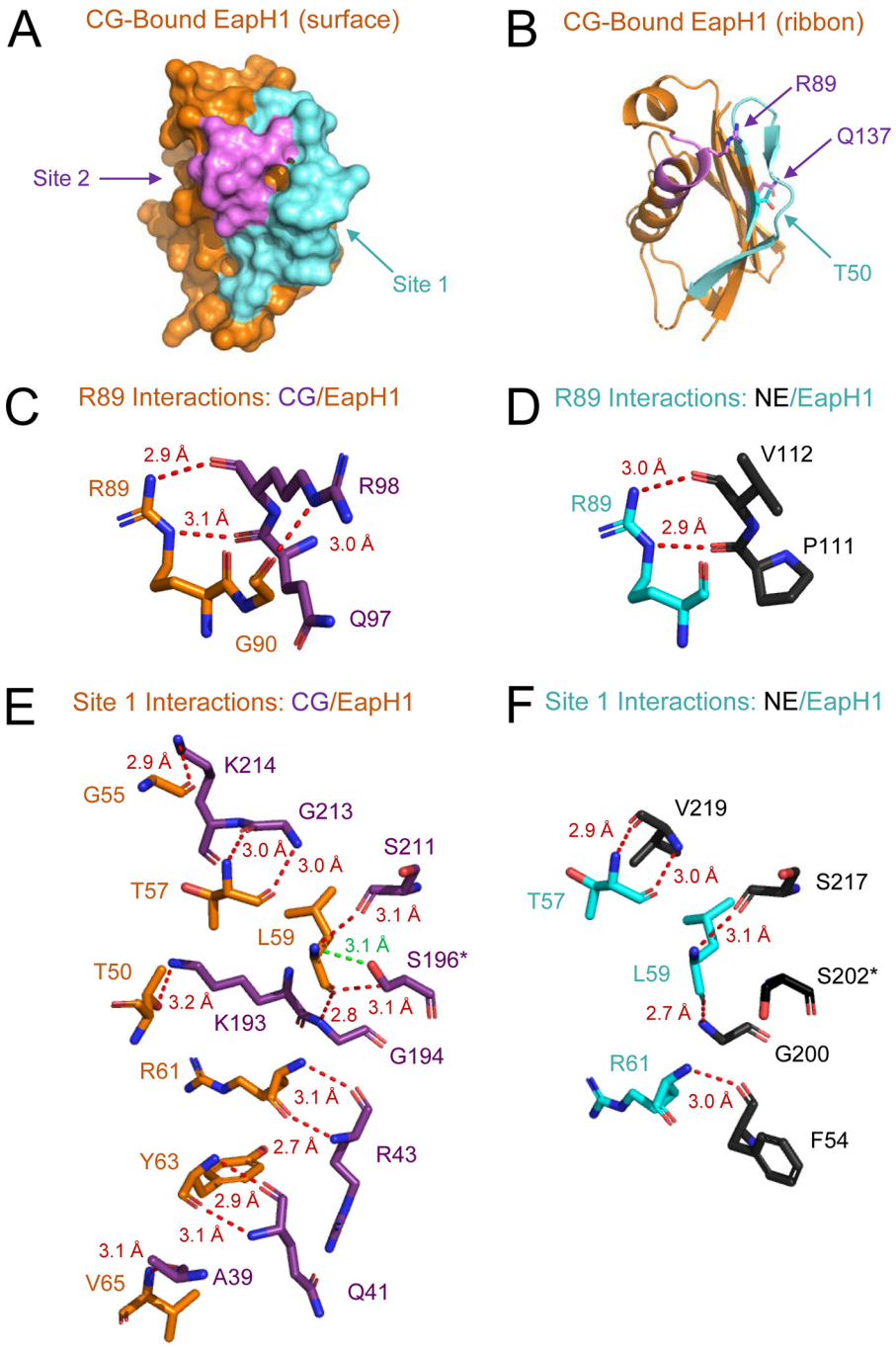

Figure 5. Comparison of EapH1 in the cathepsin-G and neutrophil elastase-bound forms reveals a high level of structural plasticity in its intermolecular interactions. *A*, surface representation of EapH1 (*orange*) and the residues found at the interface with CG in the CG/EapH1 structure. The interfacing residues are primarily derived from two different regions of EapH1, termed site 1 (Tyr^{49}–Val^{65}, *cyan*) and site 2 (Lys^{80}–Thr^{92}, *purple*). *B*, an alternative depiction of EapH1 in an identical orientation to *A*, except that protein is shown as a ribbon diagram. EapH1 residues whose side chains participate in hydrogen bonds with groups derived from CG are shown in ball-and-stick convention. *C*, hydrogen bonds formed by Arg^{89} and Gly^{90} of EapH1 in the CG-bound form. Carbon atoms from EapH1 are colored *orange*, whereas carbon atoms from CG are colored purple. *D*, hydrogen bonds formed by Arg^{89} of EapH1 in the NE-bound form. Carbon atoms from EapH1 are colored *cyan*, whereas carbon atoms from NE are colored *black*. *E*, polar interactions found at the interface between EapH1 and CG. The color scheme is identical to that in *C*. Note that the hydrogen bond between the backbone nitrogen of EapH1 Leu^{59} and the side chain of the catalytic serine, CG Ser^{196}, is highlighted in *green*. *F*, polar interactions found at the interface between EapH1 and NE viewed from an identical orientation to *E*. The color scheme is identical to *D*. Images of the NE/EapH1 structure were rendered from PDB entry 4NZL (21).

serine side chain, this interaction might exist to some degree in both complexes because the electron density maps suggest that the catalytic serine side chain for both NSPs might adopt two different rotamers. However, regardless of the rotamer, this side chain simply lies too far away to cleave the EapH1 polypeptide at Leu^{59}. Second, the interface regions between EapH1 and both NSPs are characterized by very low atomic displacement factors (Fig. S2). This strongly suggests that the residues in this area are well-ordered in the bound state and thereby restricted from undergoing large-scale changes in overall motion. Because the catalytic serine lies too far from the EapH1 backbone to cleave its peptide bond (as described above), the overall

lack of motion in this area might ensure that the NSP remains trapped in an inhibited state at the microscopic level, whereas slow dissociation rates of these complexes on the order of 10^{-4}–10^{-5} s^{-1} may serve the same purpose on the macroscopic level (k_{-4}; Table 1 and Ref. 26). Finally, the model of NE/EapH1 contains a chain break in the inhibitor at positions Glu^{68}–Asn^{69} (Fig. 4). A similar chain break is also found in all four models of the CG/EapH1 complex (Fig. 3). In each of these cases, the chain break is due to weak electron density covering the Glu^{68}–Asn^{69} region of EapH1. It is noteworthy, however, that the model for unbound EapH1 is complete throughout this region and includes both residues modeled with reasonable B-factors (22). Although the reason behind this change from the unbound to bound state is presently unclear, we suspect that it could reflect a conserved entropic contribution that helps drive high-affinity binding of EapH1 to various NSPs. We believe exploring this idea through direct experimentation might be an attractive topic for future investigation.

Although the results presented here show that EapH1 uses a globally similar ligand-binding mode to recognize two different NSPs (Fig. 4), we recently provided evidence suggesting an altogether different NE-binding mode by the EAP domain protein, EapH2 (25). Because no crystal structure was available for NE/EapH2, we used computational modeling to provide initial insight into this complex (25, 27). This model and our subsequent residue-level investigations identified positions Thr^{125} and Tyr^{127} of EapH2 as being responsible for high-affinity binding to NE (27). These EapH2 residues lie on the opposite side of the EAP domain from site 1 and site 2 discussed here (Fig. 5), thereby demonstrating that EAP domains can interact with target proteins through different high-affinity binding modes. In this regard, the individual domains comprising full-length Eap likewise exhibit potent NSP-inhibitory activity (21). However, the physical basis for their activities remains largely unexplored at this time. Given the surprising outcome of our studies on EapH2 described above (25, 27), we suspect that analogous investigations into the individual domains of Eap may reveal as yet unappreciated structural and functional properties of this remarkable family of staphylococcal innate immune evasion proteins.

We demonstrated in earlier work that all three EAP domain proteins are required for maximal virulence in a murine liver abscess model of *S. aureus* infection (21). Because these three proteins (*i.e.* Eap, EapH1, and EapH2) each individually inhibit the activities of the three canonical murine NSPs (21), we believe that this functionally redundant network of protease inhibitors is a crucial aspect of *S. aureus* innate immune evasion *in vivo*. Our discovery that EapH1 binds and inhibits human NE with ~466-fold greater potency than human CG argues that NE is the primary target of EapH1 activity in human infectious disease settings (Table 1 and Ref. 26). Nevertheless, the structure/function studies on EapH1 we have presented here and elsewhere (21, 25–27) have provided valuable illustrations of how a single member of this innate immune evasion protein family can form (sub-)nanomolar affinity inhibitory interactions with structurally related targets of limited sequence identity.

Experimental procedures

Protein preparation and purification

Human cathepsin-G (catalog no. IHUCTSG1MG) was isolated from human neutrophils and obtained from Innovative Research (Novi, MI). The enzyme was stored at 4 °C in a buffer of 50 mM sodium acetate (pH 5.5), 0.8 M NaCl and handled according to the manufacturer's suggestions unless otherwise noted. Recombinant *S. aureus* EapH1 and its R89M mutant were produced in *Escherichia coli* strain BL21(DE3) using plasmids derived from the parental expression vector pT7HMT (26, 28). All recombinant proteins were expressed as N-terminally His-tagged precursors, isolated in soluble form according to standard approaches, and digested with TEV protease to remove the affinity tag as described elsewhere (26, 28). Final purification was achieved by size-exclusion chromatography in a buffer of PBS (pH 7.4) using a Superdex 75 26/60 column connected to an AKTA FPLC system (GE Life Sciences) (26). All protein concentrations were determined using a DS-11 spectrophotometer (Denovix, Inc.) and calculated extinction coefficients.

Reversible behavior of EapH1 inhibition of human cathepsin-G

To probe the reversible nature of EapH1 inhibition of cathepsin-G, 900 nM CG was preincubated with 13.45 μM EapH1 and then diluted to a final concentration of 10.2 nM CG, 154 nM EapH1 with 50 mM HEPES (pH 7.4), 140 mM NaCl, 0.05% (v/v) Triton X-100, and 30% (v/v) DMSO containing 1.143 mM succinyl-Ala-Ala-Pro-Phe-*p*-nitroanilide (SA_2PF-pNA; Sigma–Aldrich). The reaction was followed at 400 nm for 150 min. As a control, the reaction was also followed without the preincubation of enzyme and inhibitor. In this scenario, the concentrations of enzyme and inhibitor were the same as the preincubation concentrations postdilution.

Steady-state kinetics of human cathepsin-G and inhibition by EapH1 proteins

Progress curves were collected for 30 min using a VersaMax tunable microplate reader (Molecular Devices). A total of 30 progress curves were collected for each inhibitor (two CG concentrations (~21.8 and 32.6 nM), three substrate concentrations (~ 0.28 × K_m, 0.83 × K_m, and 1.4 × K_m) per CG concentration, five inhibitor concentrations per substrate concentration). The data were fit to a rapid-equilibrium competitive inhibition mechanism (Scheme 1) using KinTek Explorer (29).

$$E + S \underset{k_{-1}}{\overset{k_1}{\longleftrightarrow}} ES \xrightarrow{k_2} EP \underset{k_{-3}}{\overset{k_3}{\longleftrightarrow}} E + P$$

$$E + I \underset{k_{-4}}{\overset{k_4}{\longleftrightarrow}} EI$$

Scheme 1

To decrease the search space of fitting the progress curves, the substrate off-rate (k_{-1}) was linked to the on-rate (k_1) by the estimated Michaelis constant (K_m) as determined by steady-

state kinetic analysis using the plate-based assay (Fig. S1). The inhibition constant was calculated from the on- and off-rate estimates determined from the fits. The values reported in Table 1 are the average of either six (EapH1-WT) or three (EapH1-R89M) sets of data, whereas the errors are the standard deviation.

Crystallization, structure determination, and refinement

A sample of human cathepsin-G inhibited by EapH1 was prepared by mixing stoichiometric amounts of each protein. The sample was then buffer exchanged into 10 mM HEPES (pH 7.5), 50 mM NaCl using a 3-kDa molecular mass cutoff ultrafiltration device and concentrated to 5 mg/ml total protein, as judged by absorbance at 280 nm. All protein concentrations were determined using theoretical extinction coefficients calculated for a 1:1 complex.

Crystals of the CG/EapH1 complex were obtained from vapor diffusion in a sitting drop format. 300 nl of protein sample were mixed with 100 nl of a precipitant solution (0.2 M lithium sulfate monohydrate, 0.1 M Tris (pH 8.5), 25% (w/v) PEG-3350) and equilibrated alongside a reservoir consisting of 50 μl of precipitant solution at 20 °C. A single crystal appeared after 10 days and grew to its final size over the course of approximately 2 months. Equivalent results were also obtained using a precipitant solution where 0.1 M HEPES (pH 7.5) was used instead of 0.1 M Tris (pH 8.5). The matured crystal was cryopreserved by briefly soaking in a buffer consisting of precipitant solution supplemented with 10% (v/v) PEG-400 prior to flash-cooling in liquid N_2.

X-ray diffraction data were collected from radiation of 0.97243 Å wavelength using Beamline 22-ID of the Advanced Photon Source (Argonne National Laboratory). Reflections were indexed in the space group *P*1, integrated and scaled using the HKL-2000 package (30). The structure was solved by molecular replacement using the refined coordinates of human cathepsin-G (PDB entry 1AU8) and hNE-bound EapH1 (PDB entry 4NZL (21)) as sequential search models in PHASER (31) as implemented within the PHENIX software suite (32, 33). The model was completed through a combination of automated and manual rebuilding, followed by positional and B-factor refinement using PHENIX.REFINE (32, 33).

The final model consists of four complexes of cathepsin-G bound to EapH1, 13 sulfate ions, and 1,026 ordered solvent molecules. The four enzyme/inhibitor complexes are essentially indistinguishable from one another, as judged by Cα superpositions on the complex represented by chains A (CG) and B (EapH1) with RMSD values of 0.167 Å (chains C and F), 0.155 Å (chains D and E), and 0.178 Å (chains G and H), respectively. The models for each copy of cathepsin-G (chains A, C, D, and G) consist of residues 16–238 inclusive, whereas the models for each copy of EapH1 (chains B, F, E, and H) consist of residues 44–141 where positions 68–69 could not be modeled because of poor map quality. 98.24% of the modeled polypeptide residues lie in favored regions of the Ramachandran plot, with only 0.16% of residues found in areas classified as outliers. A quantitative description of the cell constants, diffraction data quality, and properties of the final model for the CG/EapH1 complex can be found in Table 2.

Sequence alignments and structural analyses

A sequence alignment of human neutrophil elastase and cathepsin-G was obtained using Clustal Omega and the default settings of the software (34). This alignment, along with the program EsPript (35), was used to prepare a representation of the secondary structure features of neutrophil elastase and cathepsin-G. Three-dimensional structural analyses, including calculation of buried surface areas and identification of potential hydrogen bonds, were performed using EBI-PISA (RRID:SCR_015749) and LigPlot (36). Surface complementarity was calculated using the program *sc* (37). Structural superpositions were calculated by PyMOL, as were all renderings of protein structures from PDB files (RRID:SCR_000305).

Author contributions—T. J. H., D. A. C. S., S. H. M. R., and B. V. G. conceptualization; T. J. H. and B. V. G. data curation; T. J. H. and B. V. G. formal analysis; T. J. H., D. A. C. S., S. H. M. R., and B. V. G. investigation; T. J. H. and B. V. G. methodology; T. J. H., D. A. C. S., S. H. M. R., and B. V. G. writing-original draft; D. A. C. S., S. H. M. R., and B. V. G. writing-review and editing; S. H. M. R. and B. V. G. funding acquisition; B. V. G. supervision; B. V. G. validation; B. V. G. project administration.

Acknowledgments—X-ray diffraction data were collected at Southeast Regional Collaborative Access Team 22-ID Beamline at the Advanced Photon Source, Argonne National Laboratory. A list of supporting institutions will be provided upon request. Use of the Advanced Photon Source was supported by the U.S. Department of Energy, Office of Science, Office of Basic Energy Sciences, under Contract W-31-109-Eng-38.

References

1. Nauseef, W. M. (2007) How human neutrophils kill and degrade microbes: an integrated view. *Immunol. Rev.* **219,** 88–102 CrossRef Medline
2. Faurschou, M., and Borregaard, N. (2003) Neutrophil granules and secretory vesicles in inflammation. *Microbes Infect.* **5,** 1317–1327 CrossRef Medline
3. Amulic, B., Cazalet, C., Hayes, G. L., Metzler, K. D., and Zychlinsky, A. (2012) Neutrophil function: from mechanisms to disease. *Annu. Rev. Immunol.* **30,** 459–489 CrossRef Medline
4. Nauseef, W. M. (2014) Myeloperoxidase in human neutrophil host defense. *Cell Microbiol.* **16,** 1146–1155 CrossRef Medline
5. Korkmaz, B., Horwitz, M. S., Jenne, D. E., and Gauthier, F. (2010) Neutrophil elastase, proteinase 3, and cathepsin G as therapeutic targets in human disease. *Pharmacol. Rev.* **62,** 726–759 CrossRef Medline
6. Pham, C. T. (2006) Neutrophil serine proteases: specific regulators of inflammation. *Nat. Rev. Immunol.* **6,** 541–550 CrossRef Medline
7. Stapels, D. A., Geisbrecht, B. V., and Rooijakkers, S. H. (2015) Neutrophil serine proteases in antibacterial defense. *Curr. Opin. Microbiol.* **23,** 42–48 CrossRef Medline
8. Odeberg, H., and Olsson, I. (1976) Microbicidal mechanisms of human granulocytes: synergisitc effects of granulocyte elastase and myeloperoxidase or chymotrypsin-like cationic protein. *Infect. Immun.* **14,** 1276–1283 CrossRef Medline
9. Perera, N. C., Schilling, O., Kittel, H., Back, W., Kremmer, E., and Jenne, D. E. (2012) NSP4, an elastase-related protease in human neutrophils with arginine specificity. *Proc. Natl. Acad. Sci. U.S.A.* **109,** 6229–6234 CrossRef Medline
10. Hellman, L., and Thorpe, M. (2014) Granule proteases of hematopoietic cells, a family of versatile inflammatory mediators: an update on their cleavage specificity, *in vivo* substrates, and evolution. *Biol. Chem.* **395,** 15–49 CrossRef Medline

11. Wright, C. D., Kennedy, J. A., Zitnik, R. J., and Kashem, M. A. (1999) Inhibition of murine neutrophil serines proteinases by human and murine secretory leukocytes protease inhibitor. *Biochem. Biophys. Res. Commun.* **254,** 614–617 CrossRef Medline
12. Navia, M. A., McKeever, B. M., Springer, J. P., Lin, T. Y., Williams, H. R., Fluder, E. M., Dorn, C. P., and Hoogsteen, K. (1989) Structure of human neutrophil elastase in complex with a peptide chloromethyl ketone inhibitor at 1.84-A resolution. *Proc. Natl. Acad. Sci. U.S.A.* **86,** 7–11 CrossRef Medline
13. Hof, P., Mayr, I., Huber, R., Korzus, E., Potempa, J., Travis, J., Powers, J. C., and Bode, W. (1996) The 1.8 A crystal structure of human cathepsin G in complex with Suc-Val-Pro-PheP-(OPh)2: a Janus-faced proteinase with two opposite specificities. *EMBO J.* **15,** 5481–5491 CrossRef Medline
14. Fujinaga, M., Chernaia, M. M., Halenbeck, R., Koths, K., and James, M. N. (1996) The crystal structure of PR3, a neutrophil serine proteinase antigen of Wegener's granulomatosis antibodies. *J. Mol. Biol.* **261,** 267–278 CrossRef Medline
15. Lin, S. J., Dong, K. C., Eigenbrot, C., van Lookeren Campagne, M., and Kirchhofer, D. (2014) Structures of neutrophil serine protease 4 reveal an unusual mechanism of substrate recognition by a trypsin-fold protease. *Structure* **22,** 1333–1340 CrossRef Medline
16. Garcia, B. L., Zwarthoff, S. A., Rooijakkers, S. H., and Geisbrecht, B. V. (2016) Novel evasion mechanisms of the classical complement pathway. *J. Immunol.* **197,** 2051–2060 CrossRef Medline
17. Kim, H. K., Thammavongsa, V., Schneewind, O., and Missiakas, D. (2012) Recurrent infections and immune evasion strategies of *Staphylococcus aureus*. *Curr. Opin. Microbiol.* **15,** 92–99 CrossRef Medline
18. Lambris, J. D., Ricklin, D., and Geisbrecht, B. V. (2008) Complement evasion by human pathogens. *Nat. Rev. Microbiol.* **6,** 132–142 CrossRef Medline
19. Spaan, A. N., Surewaard, B. G., Nijland, R., and van Strijp, J. A. (2013) Neutrophils *versus Staphylococcus aureus*: a biological tug of war. *Annu. Rev. Microbiol.* **67,** 629–650 CrossRef Medline
20. Thwaites, G. E., and Gant, V. (2011) Are bloodstream leukocytes Trojan horses for the metastasis of *Staphylococcus aureus*? *Pathogens* **9,** 215–222 CrossRef Medline
21. Stapels, D. A., Ramyar, K. X., Bischoff, M., von Köckritz-Blickwede, M., Milder, F. J., Ruyken, M., Eisenbeis, J., McWhorter, W. J., Herrmann, M., van Kessel, K. P., Geisbrecht, B. V., and Rooijakkers, S. H. (2014) *Staphylococcus aureus* secretes a novel class of neutrophil-serine-protease inhibitors that promote bacterial infection. *Proc. Natl. Acad. Sci. U.S.A.* **111,** 13187–13192 CrossRef Medline
22. Geisbrecht, B. V., Hamaoka, B. Y., Perman, B., Zemla, A., and Leahy, D. J. (2005) The crystal structures of EAP domains from *Staphylococcus aureus* reveal an unexpected homology to bacterial superantigens. *J. Biol. Chem.* **280,** 17243–17250 CrossRef Medline
23. Jönsson, K., McDevitt, D., McGavin, M. H., Patti, J. M., and Höök, M. (1995) *Staphylococcus aureus* expresses a major histocompatibility complex class II analog. *J. Biol. Chem.* **270,** 21457–21460 CrossRef Medline
24. de Jong, N. W. M., Ramyar, K. X., Guerra, F. E., Nijland, R., Fevre, C., Voyich, J. M., McCarthy, A. J., Garcia, B. L., van Kessel, K. P. M., van Strijp, J. A. G., Geisbrecht, B. V., and Haas, P. A. (2017) Immune evasion by a staphylococcal inhibitor of myeloperoxidase. *Proc. Natl. Acad. Sci. U.S.A.* **114,** 9439–9444 CrossRef Medline
25. Stapels, D. A. C., Woehl, J. L., Milder, F. J., Tromp, A. T., van Batenburg, A. A., de Graaf, W. C., Broll, S. C., White, N. M., Rooijakkers, S. H. M., and Geisbrecht, B. V. (2018) Evidence for multiple modes of neutrophil serine protease recognition by the EAP family of staphylococcal innate immune evasion proteins. *Protein Sci.* **27,** 509–522 CrossRef Medline
26. Herdendorf, T. J., and Geisbrecht, B. V. (2018) Investigation of human neutrophil elastase inhibition by *Staphylococcus aureus* EapH1: the key role played by arginine 89. *Biochemistry* **57,** 6888–6896 CrossRef Medline
27. Herdendorf, T. J., and Geisbrecht, B. V. (2019) *Staphylococcus aureus* Evasion Proteins EapH1 and EapH2: residue-level investigation of an alternative binding motif for human neutrophil elastase. *Arch. Biochem. Biophys.* **676,** 108140 CrossRef Medline
28. Geisbrecht, B. V., Bouyain, S., and Pop, M. (2006) An optimized system for the expression and purification of secreted bacterial proteins. *Protein Expr. Purif.* **46,** 23–32 CrossRef Medline
29. Johnson, K. A. (2009) Fitting enzyme kinetic data with KinTek Explorer. *Methods Enzymol.* **467,** 601–626 CrossRef Medline
30. Otwinowski, Z., and Minor, W. (1997) Processing of X-ray diffraction data collected in oscillation mode. *Methods Enzymol.* **276,** 307–326 CrossRef Medline
31. McCoy, A. J., Grosse-Kunstleve, R. W., Adams, P. D., Winn, M. D., Storoni, L. C., and Read, R. J. (2007) Phaser crystallographic software. *J. Appl. Crystallogr.* **40,** 658–674 CrossRef Medline
32. Adams, P. D., Grosse-Kunstleve, R. W., Hung, L.-W., Ioerger, T. R., McCoy, A. J., Moriarty, N. W., Read, R. J., Sacchettini, J. C., Sauter, N. K., and Terwilliger, T. C. (2002) PHENIX: building new software for automated crystallographic structure determination. *Acta Crystallogr. D* **58,** 1948–1954 CrossRef Medline
33. Adams, P. D., Afonine, P. V., Bunkóczi, G., Chen, V. B., Davis, I. W., Echols, N., Headd, J. J., Hung, L. W., Kapral, G. J., Grosse-Kunstleve, R. W., McCoy, A. J., Moriarty, N. W., Oeffner, R., Read, R. J., Richardson, D. C., *et al.* (2010) PHENIX: a comprehensive Python-based system for macromolecular structure solution. *Acta Crystallogr. D Biol. Crystallogr.* **66,** 213–221 CrossRef Medline
34. Sievers, F., Wilm, A., Dineen, D., Gibson, T. J., Karplus, K., Li, W., Lopez, R., McWilliam, H., Remmert, M., Söding, J., Thompson, J. D., and Higgins, D. G. (2011) Fast, scalable generation of high-quality protein multiple sequence alignments using Clustal Omega. *Mol. Syst. Biol.* **7,** 539 CrossRef Medline
35. Robert, X., and Gouet, P. (2014) Deciphering key features in protein structures with the new ENDscript server. *Nucleic Acids Res.* **42,** W320–W324 CrossRef Medline
36. Wallace, A. C., Laskowski, R. A., and Thornton, J. M. (1995) LIGPLOT: a program to generate schematic diagrams of protein–ligand interactions. *Protein Eng.* **8,** 127–134 CrossRef Medline
37. Lawrence, M. C., and Colman, P. M. (1993) Shape complementarity at protein/protein interfaces. *J. Mol. Biol.* **234,** 946–950 CrossRef Medline

ASBMB